Journal of Materials Chemistry B

PAPER

View Article Online
View Journal | View Issue

Cite this: J. Mater. Chem. B, 2024, 12, 8349

Study of transient absorption spectroscopy of a D–π–A structure aggregation-induced emission luminogen and its photodynamic therapy application†

Siwei Zhang, ‡[a] Junqiao Wang,‡[b] Zaiyu Wang,‡[a] Ming Shao,[c] Chen Zhang,[d] Xinmeng Chen,[a] Jianwei Sun, [a] Ryan Tsz Kin Kwok,*[a] Jacky Wing Yip Lam *[a] and Ben Zhong Tang *[ae]

Photodynamic therapy (PDT) represents an emerging and noninvasive modality that has gained clinical approval for the treatment of cancers, leveraging photosensitizers for optimal therapeutic efficacy. In this study, we synthesized a photosensitizer (denoted as DTCSPP) exhibiting a donor–π–acceptor (D–π–A) structural motif. The DTCSPP manifests aggregation-induced emission (AIE) characteristics, along with good biocompatibility and mitochondrial targeting capabilities attributed to its intrinsic charge and D–π–A architecture. The excited-state intramolecular charge transfer of DTCSPP was systematically investigated in both solution and aggregate states using femtosecond transient absorption spectroscopy (fs-TA). The fs-TA results revealed that DTCSPP exhibited a more rapid and facile excited-state molecular motion in the solution state compared to the aggregate state, implying the predominance of nonradiative decay in its photophysical processes within the solution. Given its ability to simultaneously generate type I and type II reactive oxygen species and induce ferroptosis and autophagy in cancer cells, DTCSPP demonstrates effectiveness in PDT at both cellular and *in vivo* levels. This study contributes a comprehensive understanding of the excited-state intramolecular charge transfer dynamics of charged D–π–A type AIE photosensitizers, shedding light on their potential application in PDT. The multifaceted capabilities of DTCSPP underscore its promise in advancing the field of anticancer therapeutics, providing valuable insights for the identification of anticancer targets and the development of novel drugs.

Received 30th May 2024,
Accepted 20th July 2024

DOI: 10.1039/d4tb01175a

rsc.li/materials-b

1. Introduction

Photodynamic therapy (PDT) has emerged as a noninvasive therapeutic modality, and has garnered clinical approval for cancer treatment since its initial success in managing bladder cancer in 1976.[1,2] Effective PDT relies on three essential elements: photosensitizers, oxygen, and light. The photosensitizer enriched in the tumor site can be activated by light, and the relaxation process of electrons from the lowest unoccupied molecular orbital (LUMO) to the highest occupied molecular orbital (HOMO) is accompanied by generation of the reactive oxygen species (ROS), leading to localized cell death and tissue devastation. Photosensitizers can be divided into two categories based on their mechanism of action. Type I photosensitizers can react directly with the substrate by electron transfer to produce a ROS like superoxide anion radical ($^{\bullet}O_2^-$), a hydroxyl radical ($^{\bullet}OH$), and hydrogen peroxide (H_2O_2). In comparison, type II photosensitizers can react with molecular oxygen to form singlet oxygen ($^1O_2$) by energy transfer.[3] Photosensitizers, possessing high biocompatibility and remarkable ROS generation efficiency, play a crucial role in the successful implementation of PDT treatment.

Aggregation-induced emission luminogens (AIEgens) typically show weak fluorescence or nonfluorescence in the solution state but enhanced emission in the aggregate form.[4] AIEgens

[a] Department of Chemistry, Hong Kong Branch of Chinese National Engineering Research Center for Tissue Restoration and Reconstruction, Division of Life Science and State Key Laboratory of Molecular Neuroscience, The Hong Kong University of Science and Technology, Kowloon 999077, Hong Kong, China. E-mail: chryan@ust.hk, chjacky@ust.hk, tangbenz@cuhk.edu.cn
[b] Open FIESTA, Shenzhen International Graduate School, Tsinghua University, Shenzhen, 518055, China
[c] Department of Central Laboratory, the Second Affiliated Hospital, School of Medicine, The Chinese University of Hong Kong, Shenzhen & Longgang District People's Hospital of Shenzhen, Shenzhen, 518172, China
[d] The State Key Laboratory of Chemical Oncogenomics, Shenzhen International Graduate School, Tsinghua University, Shenzhen, 518055, China
[e] School of Science and Engineering, Shenzhen Institute of Aggregate Science and Technology, The Chinese University of Hong Kong, Shenzhen (CUHK-Shenzhen), Guangdong 518172, P. R. China

† Electronic supplementary information (ESI) available. See DOI: https://doi.org/10.1039/d4tb01175a

‡ These authors equally contributed.

generally possess a large Stokes' shift, good biocompatibility, and great luminosity, which have been certified to have great potential in biosensing,[5] imaging,[6] anticancer,[7] anti-infection,[8] and photoelectronic device applications.[9] Several AIE moieties, such as tetraphenylethylene (TPE), siloles, and cyanostilbenes, were reported.[10] Photosensitizers with AIE (AIE-PS) features are particularly promising in PDT treatment. Among them, the donor–π–acceptor (D–π–A) structure AIE-PSs adopt an intramolecular charge transfer strategy to separate the HOMO and the LUMO, which facilitates the intersystem crossing (ISC) process from the lowest singlet state (S_1) to the lowest triplet state (T_1) and enhances the ROS generation.[11] Additionally, the reduced energy gap between S_1 and T_1 (ΔE_{st}) in aggregates results from strong D–A interactions.[12] Charged AIE-PSs exhibit enhanced proximity in three-dimensional space due to electrostatic interactions between positively charged AIEgens and negatively charged biological species, suppressing nonradiative transitions.[13] Besides, the charged AIE-PSs inherit better water solubility, and they can more easily target organelles such as mitochondria.[14] Yin *et al.* reported a readily synthesized AIEgen TPA-Pyr-BP, which employs a strong electron acceptor of pyridinium and an electron donor of triphenylamine, proving an elevated electron D–A interaction and intramolecular charge transfer behavior.[15] Chen *et al.* reported two mitochondria-targeted AIE-PSs (DTCSPY and DTCSPE) with charged D–π–A structures. DTCSPY employs a comparatively rigid alkyne group capable of hindering the nonradiative transition due to intramolecular motion and exhibits a better PDT for HT22 neuron cells.[16] Hasrat *et al.* disclosed that a series of charged D–π–A AIE-PSs displayed superior photosensitivity for active HepG2 cells, sensitively detecting lipid droplets.[17] Although many such structure AIE-PSs have been reported and applied to diversiform bioapplications,[14b–18] the intramolecular charge transfer in the excited states is still insufficiently studied due to the ultrafast excited state relaxation process.[18] To design novel and effective AIE-PSs, detailed research on the excited states of charged D–π–A AIE-PSs is pending.

In this work, a twisted skeleton AIEgen (labeled as DTCSPP) with a charged D–π–A structure is synthesized. Our exploration of the relaxation process of excited states harnessed the precision of femtosecond transient absorption spectroscopy (fs-TA), unraveling the intricacies of intramolecular charge transfer. Distinctly, the solution state exhibited a swifter and more facile excited-state molecular motion than its aggregate counterpart, highlighting the preeminence of nonradiative decay in the photophysical processes of DTCSPP in the solution state. Complementary verification through electron paramagnetic resonance (EPR) measurements and fluorescent indicators confirmed the dual capability of DTCSPP in generating both type I ($^1O_2$) and type II ($^\bullet O_2$ and $^\bullet OH$) free radicals. DTCSPP showcased good mitochondrial targeting and demonstrated its efficacy for PDT at both cellular and *in vivo* levels for MDA-MB-231 cells. This inquiry not only advances our comprehension of the intramolecular charge transfer dynamics inherent in charged D–π–A structure AIE-PSs but also elucidates their potential in pushing the frontiers of PDT applications.

2. Results and discussion

2.1. Photophysical properties of DTCSPP

Introducing electron D and A groups into a π-conjugation system is an effective approach for long-wavelength emissive AIEgens. Fig. 1a delineates the molecular structure of the AIE-PS DTCSPP with a typical D–π–A structure. Within this structure, the *N*,*N*-diphenylthiophen-2-amine and 1-propylpyridin-1-ium groups serve as the donor and acceptor moieties, respectively. Bridging these components are benzene and a relatively rigid alkyne group, forming a twisted skeleton. Notably, a positive charge is localized on the pyridine nitrogen. To unravel the photophysical attributes of DTCSPP, a comprehensive analysis was conducted employing UV-vis absorption and photoluminescence (PL) spectroscopy. As shown in Fig. 1b and Fig. S1 (ESI†), DTCSPP exhibits a noticeable solvent effect due to its D–π–A structure. In dimethyl sulfoxide (DMSO), the absorption peak manifests at 497 nm, while in dioxane and dichloromethane (DCM), the peaks shift to 441 nm and 531 nm, respectively. The PL peak symmetry centers around 560 nm in DMSO, dioxane, and acetone, exhibiting redshifts and broadening in tetrahydrofuran (THF) and DCM. Delving further into the AIE characteristics of DTCSPP in varying DMSO and water fractions (f_{water}) in Fig. 1c and d, it is evident that the fluorescence intensity in pure DMSO is relatively subdued. However, with an increase in f_{water}, the PL intensity experiences an enhancement accompanied by a redshift, which could be caused by twisted intramolecular charge transfer and H-aggregation of the DTCSPP. Transitioning to a DMSO : water ratio of 1 : 9 prompts the formation of DTCSPP aggregate nanoparticles with a discernible particle size of 119 nm (Fig. S2, ESI†). The relative fluorescence intensity ($\alpha_{AIE} = I/I_0$) registers a remarkable twenty-fold enhancement.

Moreover, in the solid state, a mass fraction of 2% DTCSPP within a polymethyl methacrylate (PMMA) film exhibits intensified emission at 680 nm, as elucidated through time-resolved photoluminescence with a characteristic decay time of 17 ns, markedly surpassing its solution state counterpart (Fig. S3, ESI†). The heightened fluorescence intensity and prolonged lifetime observed in the aggregate state signify the mitigation of nonradiative transitions attributed to molecular motion.

2.2. Theoretical calculation and femtosecond transient absorption spectra

To gain deeper insights into the molecular structure and excited properties of DTCSPP, a density functional theory (DFT) analysis was conducted. Fig. S4 (ESI†) and Fig. 2a present the optimized geometries and electron cloud distribution. Specifically, the optimized geometry illustrates a pronounced dihedral angle within the stilbene segment, measuring 17.8°. Simultaneously, the HOMO and LUMO electron clouds exhibit a discernible spatial separation in DTCSPP. The HOMO electron cloud primarily localizes on the *N*,*N*-diphenylthiophen-2-amine moiety, whereas the LUMO electron cloud is prominently situated on the 1-propylpyridin-1-ium group. This spatial distribution implies a distinct intramolecular charge transfer excited feature within DTCSPP, accentuating its propensity for dynamic electronic transitions.

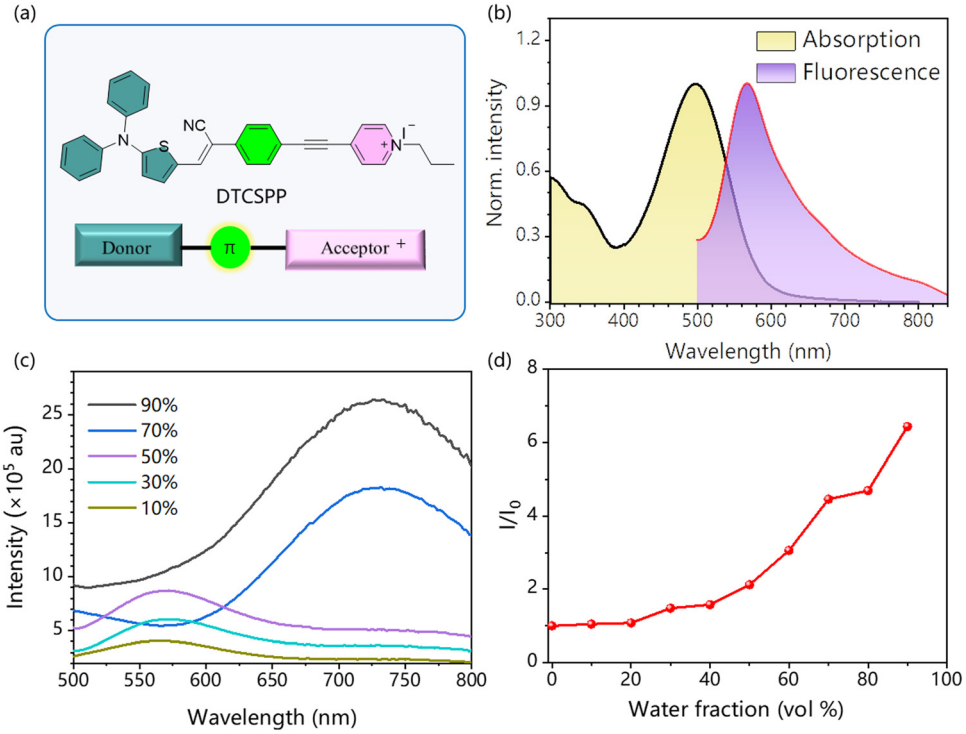

Fig. 1 (a) The molecular structure of the DTCSPP. (b) Normalized absorption and photoluminescence spectra of the DTCSPP in DMSO solution. Concentration = 10^{-5} M. (c) Fluorescence intensities of DTCSPP in DMSO/water mixtures with different water fractions (f_{water}). Concentration = 10^{-5} M, λ_{ex} = 500 nm. (d) The plot of relative PL intensity ($\alpha_{AIE} = I/I_0$) of DTCSPP in mixtures of DMSO/water with varying f_{water} (vol %).

Fs-TA with the pump–probe system can monitor the evolution of the molecular excited states at the femtosecond scale. Here, a 400 nm pump laser pulse was applied to excite the DTCSPP in both the DMSO solution state and aggregate state (mixture of DMSO : water = 1 : 9) (concentration = 10^{-5} M) to study the influence of aggregation behavior on excited states. The time-wavelength-dependent fs-TA color map (Fig. 2b and f) provides a detailed depiction of the dynamic evolution of molecular excited states. The negative induced optical density (OD) observed around 450 nm corresponds to the stimulated emission (SE) band, while the positive OD peak around 590 nm indicates Excited State Absorption (ESA). The SE process elucidates the sample's return to the ground state from an unstable excited state under the pump laser, accompanied by fluorescence generation. Meanwhile, ESA directly mirrors the internal conversion of $S_n \rightarrow S_1$ and the molecular structural alterations during the excitation process.

In the solution state, the evolution of the ESA peak from 50 to 900 fs, marked by a redshift from 480 nm to 602 nm (Fig. 2c and d), is attributed to a molecular motion process, such as the torsion of the molecular skeleton and rotation of the benzene ring. The rotation of the molecular skeleton under light induces a redshift in the absorption peak of the excited state.[19] Notably, the kinetic fitting results at 590 nm reveals a lifetime of 53.2 ps. In the aggregate state, the ESA peak evolution spans from 50 to 1200 fs, with a redshift from 486 nm to 605 nm (Fig. 2g and h), surpassing the extent observed in the solution state. The corresponding kinetic fitting results at 590 nm indicates a sluggish lifetime of 72.8 ps (Fig. 2i). This comparative analysis suggests that the solution state exhibits a faster and more facile excited-state molecular motion than the aggregate state, indicating the predominant role of nonradiative decay in the photophysical processes of DTCSPP. The aggregate state, conversely, effectively inhibits molecular motion.

2.3. ROS generation

EPR measurement was carried out to assess the generation of the ROS. Spin-trap agents 5,5-dimethyl-1-pyrroline-*N*-oxide (DMPO) and 4-amino-2,2,6,6-tetramethylpiperidine (TEMP) were adopted to trap the radical $^{\bullet}OH/^{\bullet}O_2^-$ and $^1O_2$, respectively. As illustrated in Fig. 3a–c, no discernible EPR signal was detected under dark conditions. In stark contrast, under light exposure, distinct EPR spectra corresponding to different capture agents emerged, unequivocally confirming the generation of diverse free radicals. The sharp and strong intensity of the EPR spectra attests to the high efficiency of ROS generation facilitated by DTCSPP. Furthermore, fluorescent indicators were adopted to detect the intensity of free radical generation. Indicators 9,10-anthracenedivl-bis (methylene) dimalonic acid (ABDA) and hydroxyphenyl fluorescein (HPF) were then utilized for the detection of $^1O_2$ and $^{\bullet}OH$, respectively. In comparison to the commercial photosensitizer Rose Bengal (RB), DTCSPP exhibited superior $^1O_2$ generation efficiency, as elucidated in Fig. 3d and Fig. S6 (ESI†). The relative PL intensity I/I_0 in HPF and 2,7-dichlorodihydrofluorescein diacetate (DCFH) also experienced a substantial increase of 15 times and 400 times, respectively (Fig. 3e, f and Fig. S7, ESI†). This noteworthy enhancement

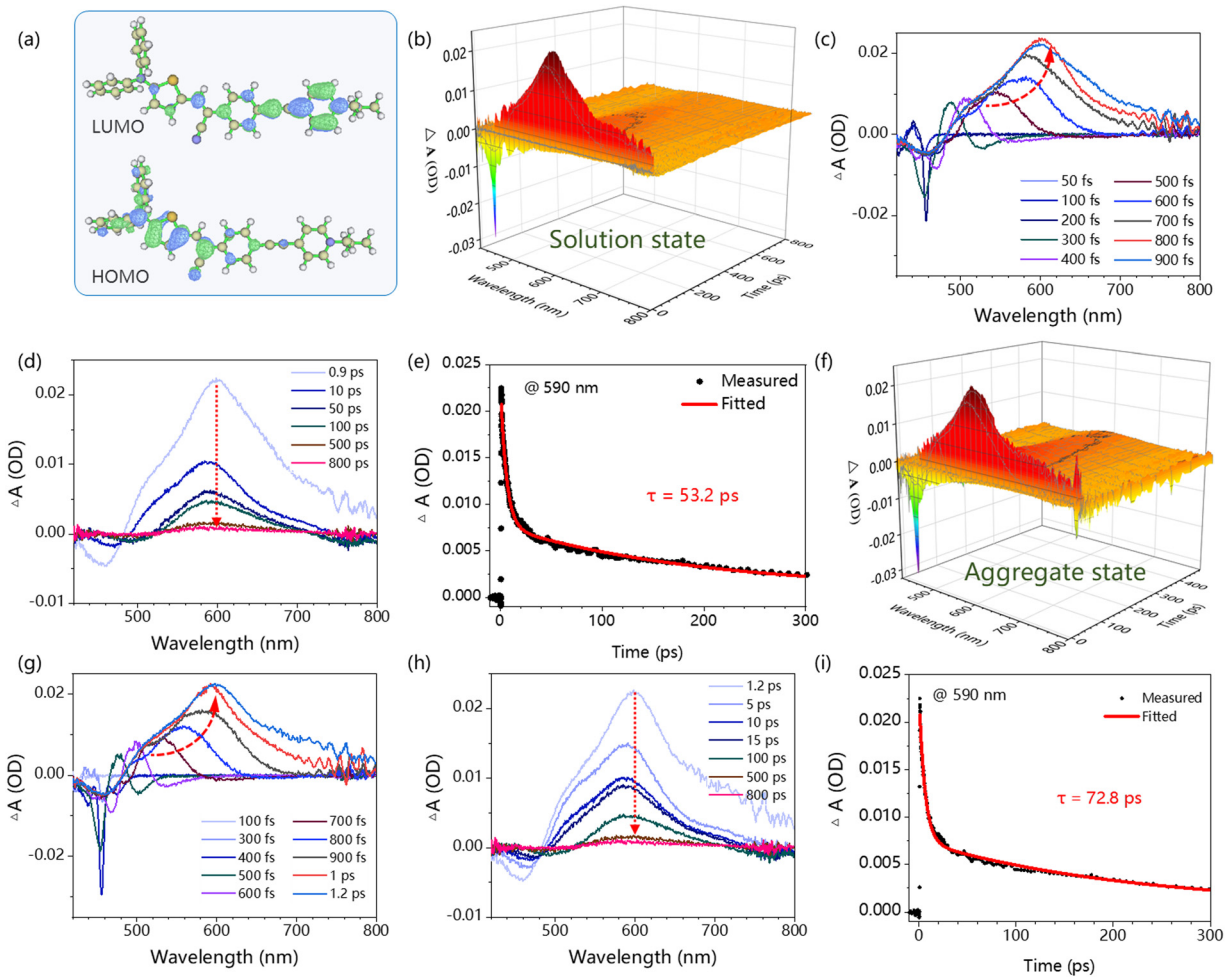

Fig. 2 (a) The DFT simulated electron cloud distributions of HOMO and LUMO at CAM-B3LYP density functional and 6-31G(d,p) basis set (the isosurface value is 0.040). The fs-TA of DTCSPP in DMSO solution: (b) the time-wavelength-dependent color maps, (c) and (d) the select fs-TA spectra. (e) The kinetic fitting of peaks at 590 nm. The fs-TA of DTCSPP in the mixture of DMSO : water = 1 : 9. (f) The time-wavelength-dependent color maps, (g) and (h) the select fs-TA spectra. (i) The kinetic fitting of peaks at 590 nm. Concentration = 10^{-5} M. The pump laser is 400 nm.

in effective ROS generation efficiency underscores the potential of DTCSPP for achieving exemplary performance in PDT. The intricate interplay between DTCSPP and various indicators unveils its capacity for robust ROS generation, positioning it as a promising candidate for efficient PDT treatments.

2.4. Intracellular ROS detection and PDT treatment

The DTCSPP can be taken up by MDA-MB-231 cells (Fig. S8, ESI†), so intracellular ROS generation can be detected utilizing a DCFH probe. Fig. 4a and d vividly illustrates that MDA-MB-231 cells subjected to PBS-only, PBS + light, and the DTCSPP-only groups exhibited negligible green fluorescence signals, indicative of a lack of ROS generation within the cellular milieu. In contrast, MDA-MB-231 cells treated with DTCSPP followed by white light irradiation displayed a pronounced green fluorescence. The quantification of relative fluorescence intensity, as depicted in Fig. 4e, unequivocally establishes that the DTCSPP + light group manifests the strongest green fluorescence, underscoring its good intracellular ROS production capacity.

The standard Cell Counting Kit-8 (CCK8) assay is also conducted using MDA-MB-231 cells to demonstrate DTCSPP cell-killing performance. As shown in Fig. 4f, under dark conditions, the cells showed good viability under the treatment of different concentrations of DTCSPP. Even at the concentration of 10 μM, almost 100% viability was guaranteed, while under light conditions, a notable decline in cell viability was observed even at lower concentrations, with 5 μM yielding less than 10% viability. Moreover, it can be estimated that the half-maximal inhibitory concentration (IC_{50}) of DTCSPP is about 2.5 μM under light, highlighting its good intracellular ROS generation capability. This comprehensive analysis underscores not only the good intracellular ROS-generating potential of DTCSPP but also its consequential impact on cell viability under light conditions.

The mitochondria-targeting ability of DTCSPP was assessed through co-staining with the commercial mitochondrial probe Mito-Tracker Deep Red. As depicted in Fig. 5a–c, the co-localization of the red emission from Mito-Tracker Deep Red and the green emission from DTCSPP demonstrated a high overlap, yielding a Pearson's correlation coefficient of 0.68.

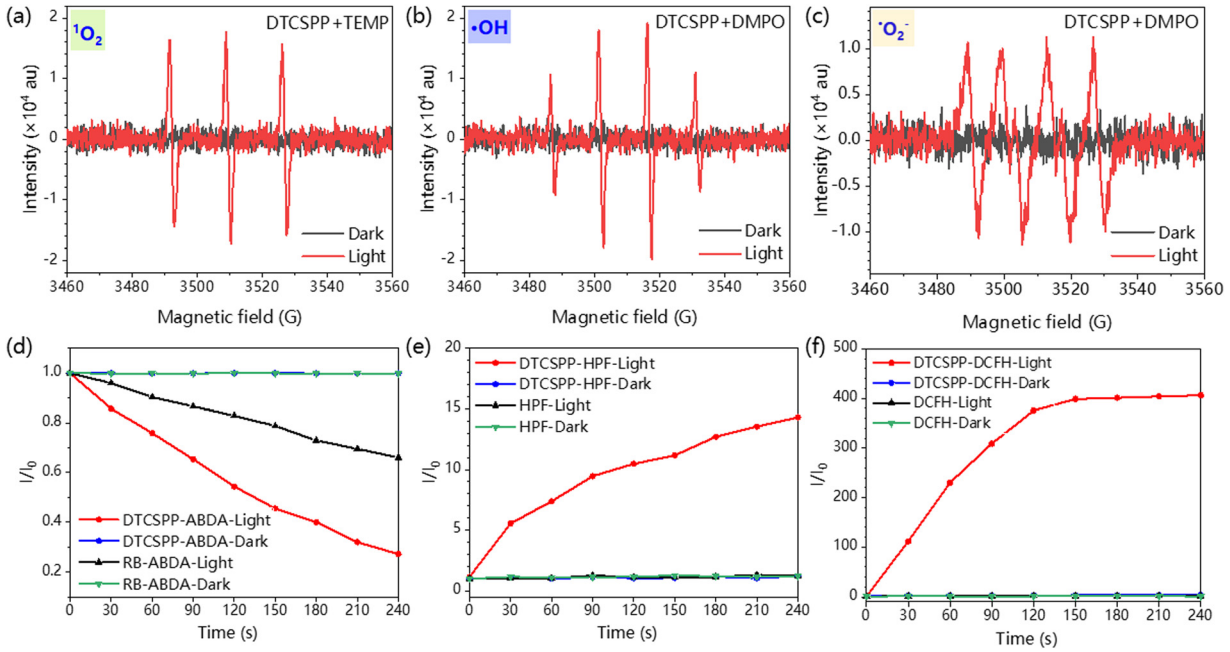

Fig. 3 EPR spectra of (a) $^1O_2$ trapped by TEMP, (b) $^{\bullet}OH$, and (c) $^{\bullet}O_2^-$ trapped by DMPO and with and without laser irradiation. The plot of relative PL intensity of (d) ABDA (for $^1O_2$ detection), (e) HPF (for $^{\bullet}OH$ detection), and (f) DCFH in the presence of 1 μM DTCSPP or Rose Bengal (RB) upon white light irradiation for 1 min.

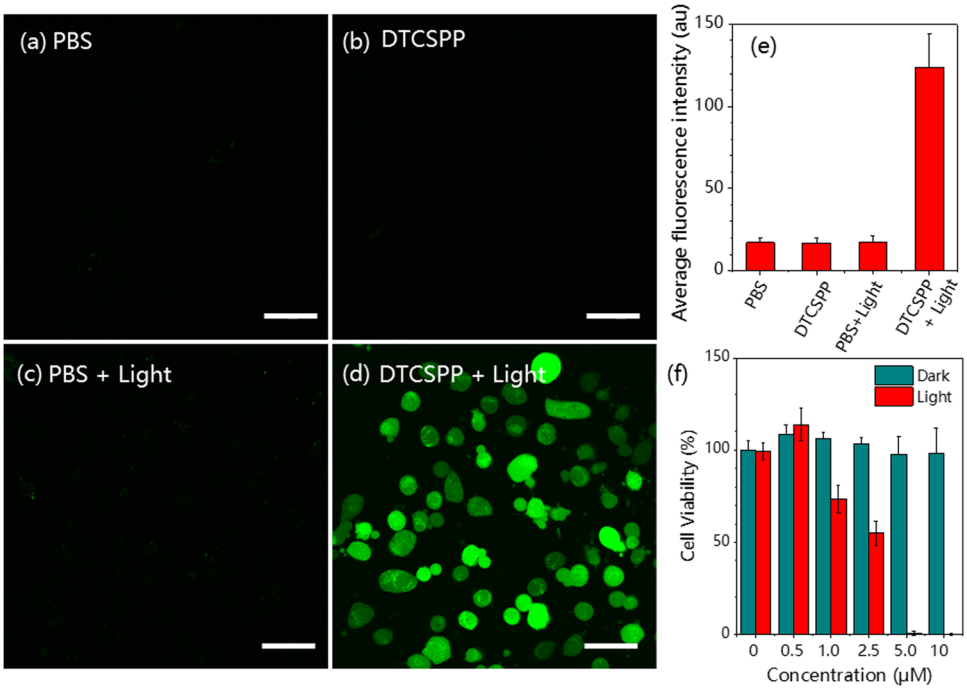

Fig. 4 MDA-MB-231 cells intracellular ROS detection using the DCFH probe under (a) PBS only, (b) PBS + light, (c) DTCSPP only, and (d) DTCSPP + light. (e) Quantitative analysis of Fig. 4a–d using ImageJ software (n = 3 for each group). (f) Cell viability of MDA-MB-231 cells after treatment with various formulations. Scale bar: 50 μm. White light intensity 50 mW cm^{-2}.

This result substantiates the good mitochondria-targeting capability of DTCSPP, further strengthening its potential as an effective therapeutic agent. Observing the morphological characteristics of MDA-MB-231 cells under various treatments, cells subjected to PBS, PBS + light, and DTCSPP only retained a spindle-shaped morphology (Fig. 5d–g). Remarkably, cells treated with DTCSPP + light exhibited a distinct rounding, with no observable membranous tissue rupture. This morphological alteration underscores the impact of DTCSPP in inducing structural changes in cancer cells. To delve deeper into the

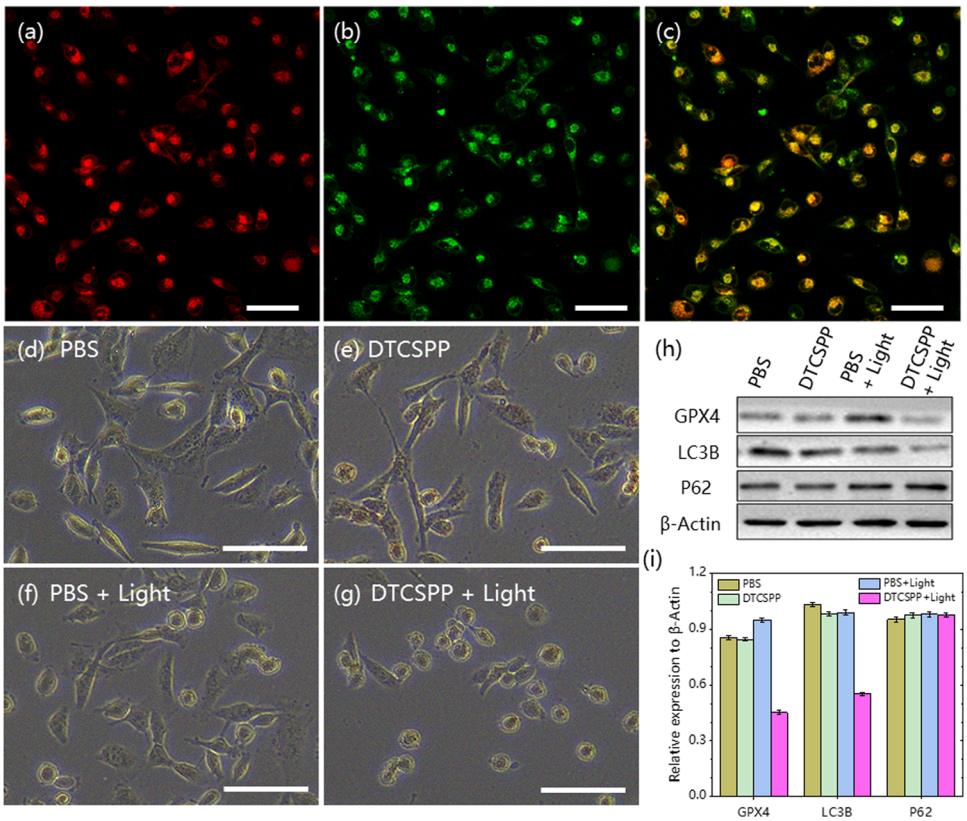

Fig. 5 Microscopy images of co-localization between (a) 5 μM DTCSPY and (b) 1 μM MTDR in MDA-MB-231 cells; (c) overlap between a and b; the MDA-MB-231 cells morphology after (d) PBS, (e) DTCSPP, (f) PBS + light, and (g) DTCSPP + light treatment. Scale bar: 100 μm. (h) The mechanism analysis of cytoprotective autophagy and ferroptosis with different treatments by western blots. (i) Quantitative analysis of GPX4, LC3B, and P62 dots in different groups.

anti-tumor mechanisms of DTCSPP, a western blot experiment was conducted, focusing on glutathione peroxidase (GPX4), LC3B, and P62 proteins, representative markers of ferroptosis and autophagy. As illustrated in Fig. 5h, i and Fig. S9 (ESI†), quantitative analysis revealed a significant downregulation of GPX4 and LC3B expression in the DTCSPP + light group. This inhibition suggests that ferroptosis and autophagy pathways may contribute to cancer cell death induced by DTCSPP.

2.5. *In vivo* anticancer studies

To assess the *in vivo* performance of the DTCSPP, a tumor-bearing mouse model was meticulously established. Six-week-old female nude mice were subcutaneously injected with a cell suspension containing 1×10^7 MDA-MB-231 cells. The tumor volume was allowed to reach approximately 100 mm^3 before initiating the *in vivo* experiment. Subsequently, the mice ($n = 3$) underwent intratumoral injection with PBS or DTCSPP (10 mg kg^{-1}) accompanied by white LED light irradiation (150 mW cm^{-2}) for 2 hours or without irradiation. As illustrated in Fig. 6a, b and Fig. S10 (ESI†), DTCSPP exhibited minimal anti-tumor effects in the absence of light stimulation, with tumor volumes and weights escalating more than six-fold after 15 days, akin to the control groups. However, under irradiation, the tumor inhibition effect was evident, resulting in nearly complete suppression of tumor growth owing to the heightened light-induced ROS production efficiencies of DTCSPP. Fig. 6c and d visually and quantitatively depicts the tumor weights following different treatments. Notably, throughout the entire PDT study, there was no noticeable change in body weight (Fig. S11, ESI†), reaffirming the low dark toxicity of DTCSPP.

The mice were sacrificed on day 15 after PDT treatment, and the tumor tissues were collected for histological analysis (Fig. 6e). All groups exhibited marked nucleus dissociation and necrosis using hematoxylin and eosin (H&E) stain, validating the effective PDT efficacy of the compounds. Collectively, these comprehensive data unequivocally establish DTCSPP's good anti-tumor effects and low biotoxicity in an *in vivo* setting, highlighting its potential as an impactful and safe therapeutic agent for cancer treatment.

3. Conclusions

In summary, we synthesized one AIE-PS with an excellent ability to generate both type I and type II ROS. With the D–π–A structure and intrinsic charge, the AIE-PS demonstrates good biocompatibility and mitochondrial targeting. We studied the charge transfer process of the excited state in the solution and aggregate state by fs-TA and certified that the nonradiative transition dominated the excited state in the solution state and was inhibited in the aggregation state. Benefits of its high

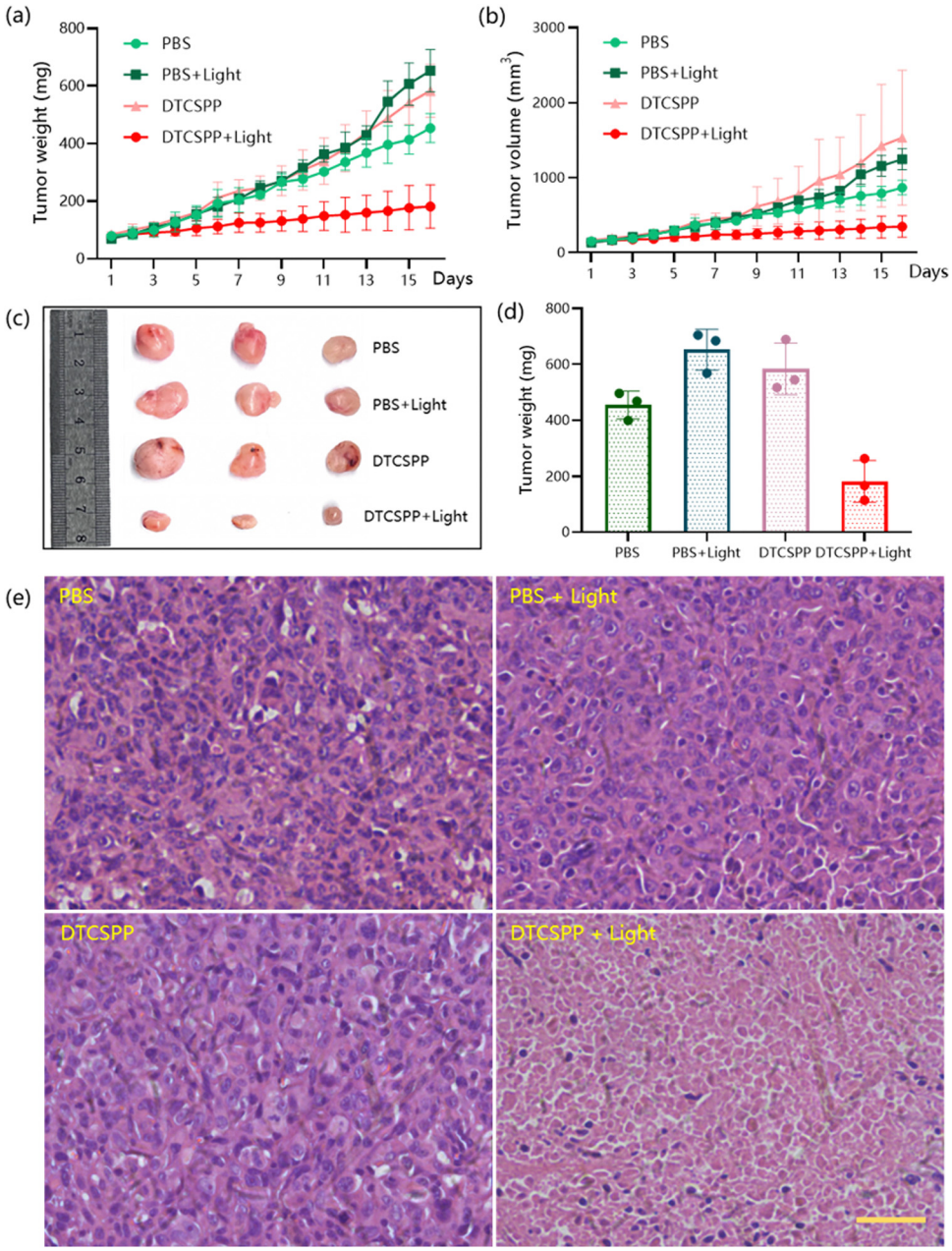

Fig. 6 *In vivo* PDT performance of DTCSPP on MDA-MB-231 tumor-bearing mice. (a) Tumor weight and (b) tumor volume during the treatment. (c) Tumor images and (d) tumor weight in different groups were obtained on the 14th day after different treatments. (e) H&E staining of tumor tissue in various treatment groups. Scale bar: 200 μm.

ROS generation capacity, DTCSPP has achieved good anti-tumor effects at both cellular and *in vivo* levels, and the mechanistic underpinnings of its anti-tumor efficacy potentially involve ferroptosis and autophagy. Our discovery provides a deeper comprehension of intramolecular charge transfer processes in excited states, gleaned from fs-TA, coupled with an understanding of how the aggregation state limits intramolecular motion, collectively propels the advancement of AIE-PSs in the realm of therapeutic development. This discovery not only enriches our knowledge of AIE-PSs but also lays a foundation for further exploration and innovation in the field.

Data availability

The data supporting this article have been included as part of the ESI.† Data will be made available on request.

Conflicts of interest

The authors declare that they have no known competing financial interests or personal relationships that could have appeared to influence the work reported in this paper.

Acknowledgements

The authors are thankful for the support of the Science Technology Innovation Commission of Shenzhen Municipality (GJHZ20210705141810031) and the Innovation and Technology Commission (ITC-CNERC14SC01 and ITCPD/17-9). We thank the Materials Characterization and Preparation Center, The Chinese University of Hong Kong, Shenzhen, for the material characterization.

References

1 D. L. Sai, J. Lee, D. L. Nguyen and Y. P. Kim, *Exp. Mol. Med.*, 2021, **53**, 495–504.
2 J. F. Kelly and M. E. Snell, *J. Urol.*, 1976, **115**, 150–151.
3 L. Zhang and D. Ding, *View*, 2021, **2**(6), 20200179.
4 (*a*) H. Wang, E. Zhao, J. W. Y. Lam and B. Z. Tang, *Mater. Today*, 2015, **18**, 365–377; (*b*) Y. Tu, Z. Zhao, J. W. Y. Lam and B. Z. Tang, *Matter*, 2021, **4**, 338–349; (*c*) Z. Zhao, H. Zhang, J. W. Y. Lam and B. Z. Tang, *Angew. Chem., Int. Ed.*, 2020, **59**, 9888–9907.
5 Y. Yu, S. W. Zhang, J. Jiang, F. Ma, R. Wang, T. Huang, J. Zhao, C. He and G. Wei, *Adv. Sensor Res.*, 2023, **2**(11), 2300027.
6 R. Zhang, P. Shen, Y. Xiong, T. Wu, G. Wang, Y. Wang, L. Zhang, H. Yang, W. He, J. Du, X. Wei, S. Zhang, Z. Qiu, W. Zhang, Z. Zhao and B. Z. Tang, *Natl. Sci. Rev.*, 2023, **11**(2), nwad286.
7 D. Yan, Y. Qin, S. Yan, P. Sun, Y. Wang, D. Wang and B. Z. Tang, *Particuology*, 2023, **74**, 103–118.
8 Y. Wu, J. Li, Z. Shen, D. Wang, R. Dong, J. Zhang, Y. Pan, Y. Li, D. Wang and B. Z. Tang, *Angew. Chem.*, 2022, 134.
9 (*a*) S. Zhang, Z. Li, J. Li, B. Wang, F. Chen, X. Li, S. Liu, J. W. Y. Lam, G. Xing, J. Li, Z. Zhao, F. Kang, G. Wei and B. Z. Tang, *Aggregate*, 2023, **4**(5), e345; (*b*) Y. Zhao, L. Zhang, Y. Liu, Z. Deng, R. Zhang, S. Zhang, W. He, Z. Qiu, Z. Zhao and B. Z. Tang, *Langmuir*, 2022, **38**, 8719–8732; (*c*) X. Y. He, H. L. Xie, L. R. Hu, P. C. Liu, C. H. Xu, W. He, W. T. Du, S. W. Zhang, H. Xing, X. Y. Liu, H. Park, T. S. Cheung, M. H. Li, R. T. K. Kwok, J. W. Y. Lam, J. Lu and B. Z. Tang, *Aggregate*, 2023, **4**, e239.
10 Z.-L. Gong, X. Zhu, Z. Zhou, S.-W. Zhang, D. Yang, B. Zhao, Y.-P. Zhang, J. Deng, Y. Cheng, Y.-X. Zheng, S.-Q. Zang, H. Kuang, P. Duan, M. Yuan, C.-F. Chen, Y. S. Zhao, Y.-W. Zhong, B. Z. Tang and M. Liu, *Sci. Chin. Chem.*, 2021, 1–45.
11 I. R. Gould, *J. Phys. Chem. A*, 2003, **107**, 3515–3524.
12 T. Zhang, J. Zhang, F. B. Wang, H. Cao, D. Zhu, X. Chen, C. Xu, X. Yang, W. Huang, Z. Wang, J. Wang, Z. He, Z. Zheng, J. W. Y. Lam and B. Z. Tang, *Adv. Funct. Mater.*, 2022, **32**(16), 2110526.
13 J. Qian and B. Z. Tang, *Chem*, 2017, **3**, 56–91.
14 (*a*) X. Liu, C. Zhu and B. Z. Tang, *Acc. Chem. Res.*, 2022, **55**, 197–208; (*b*) A. Lal Koner, D. Chopra and N. T. Patil, *ChemBioChem*, 2022, **23**, e202200320.
15 W. Yin, Z. Yang, S. Zhang, Y. Yang, L. Zhao, Z. Li, B. Zhang, S. Zhang, B. Han and H. Ma, *Mater. Chem. Front.*, 2021, **5**, 2849–2859.
16 C. Chen, R. Zhang, J. Zhang, Y. Zhang, H. Zhang, Z. Wang, X. Huang, S. Chen, R. T. K. Kwok, J. W. Y. Lam, D. Ding and B. Z. Tang, *CCS Chem.*, 2022, **4**, 2249–2257.
17 K. Hasrat, X. Wang, Y. Li, L. Yang, Y. Zhao, K. Xue, X. Wang, J. Deng, J. Liang and Z. Qi, *Dyes Pigm.*, 2023, 211.
18 (*a*) W. Li, M. Huang, Y. Li, Z. Yang and J. Qu, *Dyes Pigm.*, 2021, **186**, 109041; (*b*) Y. Yang, J.-J. Tian, L. Wang, Z. Chen and S. Pu, *J. Photochem. Photobiol., A*, 2022, **429**, 113905; (*c*) Y. Zhou, Z. Yang, Z. Qiu, N. Tang, D. Sun, B. Liu, X. Wu, S. Ji, W.-C. Chen and Y. Huo, *J. Photochem. Photobiol., A*, 2022, **428**, 113891; (*d*) J. Ni, Y. Wang, H. Zhang, J. Z. Sun and B. Z. Tang, *Molecules*, 2021, **26**(2), 268; (*e*) M. Sathiyaraj and V. Thiagarajan, *RSC Adv.*, 2020, **10**, 25848–25855.
19 H. Zhang, J. Liu, L. Du, C. Ma, N. L. C. Leung, Y. Niu, A. Qin, J. Sun, Q. Peng, H. H. Y. Sung, I. D. Williams, R. T. K. Kwok, J. W. Y. Lam, K. S. Wong, D. L. Phillips and B. Z. Tang, *Mater. Chem. Front.*, 2019, **3**, 1143–1150.